

The following is an author-produced version of an article accepted for publication in the journal Remote Sensing of Environment on January 27, 2023 (©2023 under the [CC-BY-NC-ND 4.0 license](#)). Initial submission was on March 14, 2022. The definitive version from the publisher can be cited as [Danielson, R. E., H. Shen, J. Tao, and W. Perrie, 2023: Dependence of ocean surface filaments on wind speed: An observational study of North Atlantic right whale habitat](#). All versions seek to address:

Collocations of Gulf of St. Lawrence whale sightings and synthetic aperture radar scenes
Quantification of a dependence of submesoscale filaments at the ocean surface on wind speed
Consistency in linear and nonlinear components of Pearson and distance correlation
A simple wind speed adjustment of synthetic aperture radar contrast

Dependence of ocean surface filaments on wind speed: An observational study of North Atlantic right whale habitat

Richard E. Danielson, Hui Shen, Jing Tao, and William Perrie
Bedford Institute of Oceanography, Fisheries and Oceans Canada
Dartmouth, Nova Scotia, Canada

Keywords: ocean current deformation, synthetic aperture radar, sea surface filaments

Abstract

Coherent filaments at the ocean surface often appear to be transient watermass boundaries, where currents converge, surfactants accumulate, and frontal structure at depth can possibly delineate enhanced biological activity in the upper water column. Spaceborne synthetic aperture radar (SAR) permits filaments to be observed at O[1-km] resolution, but extensive coherent structures are more apparent in weaker winds. A wind speed adjustment is proposed for filaments (i.e., contiguous SAR contrasts) of at least 10 km in length. Measures of dependence (distance correlation and the linear and nonlinear components of Pearson correlation) are examined to identify a broad peak in the relationship between filament contrast and weak or moderate values of surface wind speed, where a variable wind speed exponent is employed to maximize these measures.

Three locations of recent North Atlantic right whale (*Eubalaena glacialis*) sightings in the Gulf of St. Lawrence are sampled between 2008 and 2020 by 324 Radarsat-2 SAR scenes and 10-m wind speed from the ERA5 reanalysis. The inverse relationship between SAR contrast magnitude and wind speed is quantified, and a reduced correlation is obtained for all three domains when SAR contrast is weighted by wind speed to the power of 0.8. A more uniform emphasis on ocean surface structure within a SAR scene, or across multiple scenes, can thus be considered in the search for prey aggregations of the North Atlantic right whale.

1 Introduction

Ecosystem studies in the Gulf of St. Lawrence (GSL) are well suited to address the stock and supply of zooplankton *Calanus* spp., the preferred prey of the endangered North Atlantic right whale (NARW), *Eubalaena glacialis* (Plourde et al. 2019; Sorochan et al. 2019; Gavrilchuk et al. 2020; Brennan et al. 2021). For an animal the size of a grain of rice, however, one of the best known indications of its local aggrega-

tion (i.e., only dense aggregations of *Calanus* offer a net energy surplus to a right whale) is the right whale itself (Baumgartner et al. 2007). Observations of right whales suggest that mothers provide foraging patterns for their young and sensory perception is employed while feeding. In addition, Kenney et al. (2001) provide a number of hypotheses about how right whales might discover *Calanus* aggregations beyond their immediate locale.

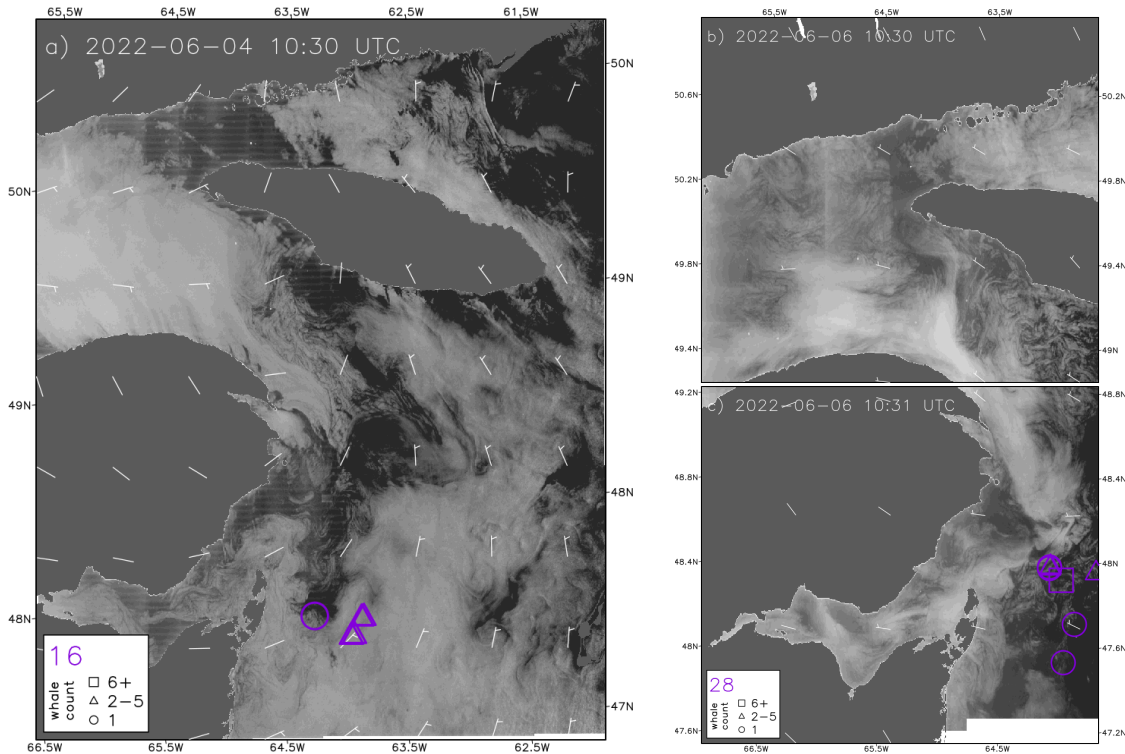


Figure 1: Synthetic aperture radar scenes from descending passes of the a) Radarsat Constellation Mission (RCM-1) and b,c) Sentinel (S-1a) satellites during a quiescent period of weak winds over the Gulf of St. Lawrence. Shown are normalized radar cross section (σ_0) at 10:30 UTC on June 4 (left) and June 6 (right), 2022. Dark and light shading denote small and large σ_0 (or smooth and rough ocean surfaces), respectively. Purple marks are sightings of NARW groups on the corresponding day, with the total number of individuals at lower left. Wind barbs are interpolated from the ERA5 reanalysis, with half barbs denoting 5 ms^{-1} .

A synthesis of *Calanus* spp. life cycle and expected biomass distributions in the GSL is given by Sorochan et al. (2021), who highlight the need to explore NARW prey aggregation at depth, as well as transient aggregation near the surface, in regions delimited by tidal mixing and freshwater pulses, and in convergent circulations in the upper mixed layer (their Fig. 5a). As with aggregation cues in complementary high-resolution satellite images (e.g. Base-

dow et al. 2019; Barthelmeß et al. 2021), the interpretation of surface roughness patterns in synthetic aperture radar (SAR) images is well developed (Holt 2004). An historical account is given by Munk et al. (2000), who address the dynamics of O[10-km] cyclonic eddies, in which coherent filaments at the ocean surface can be seen to evolve. Such developments motivate the question of whether ocean currents, fronts, waves, and eddies that are revealed in SAR roughness might be helpful to understand NARW prey aggregation.

Examples of roughness patterns that bracket two days of weak winds over the GSL are shown in Fig. 1. Dark and light shading denotes smooth and rough ocean surfaces, respectively. Filaments of all shades prevail at the smallest scales, with a transverse separation between filaments of O[10 km] or less. McWilliams et al. (2009) demonstrate that a symmetric boundary layer evolution, organized by an initially frontogenetic (e.g., eddy) circulation, can result in rapid downwelling. This is marked in SAR scenes by darker lines that are thin relative to adjacent lighter lines (e.g., east of 64.5°W). Such contrasts can also be enhanced by an accumulation of surfactants (active surface materials) of terrestrial or atmospheric origin, with sources in the water column that include bacteria, plankton, fish, and crude oil seepage (Espedal et al. 1998; Hamilton et al. 2015; Kurata et al. 2016).

Large scale patterns of surface stress are also apparent in Fig. 1. Dark regions lack the O[1-10-cm] roughness elements that cause radar backscatter, and indicate wind speeds of less than about 2 ms⁻¹ (Holt 2004). However, the southern boundary of this smooth region also seems to bound a precursor water-mass extension into the southern GSL, close to where 16 NARWs were sighted (Fig. 1a). Further upstream, a bright region along the north shore of the Gaspé Peninsula (cf. Fig. 2) suggests a relatively warm and fresh surface layer with enhanced atmospheric coupling (e.g., northward lines in Fig. 1a are likely offshore wind streaks). Within a few days (Fig. 1b), this large scale roughness contrast extends toward groups of NARWs further north. Along the boundaries of the precursor and subsequent watermasses, surface current convergence seems to exist, although as might be expected (Espedal et al. 1998; Munk et al. 2000), contrasts that bound the brighter region are not as robust as those that bound the darker region of Fig. 1. The possible role of surfactants is discussed further in Section 5.

1.1 Radar modelling

This quiescent period of weak winds is exemplary of an upper ocean current response captured by SAR snapshots. Rasle et al. (2017, 2020) further emphasize that ocean currents modulate waves and wave breaking, and in turn, surface roughness over a wide range of environmental conditions, including at wind speeds of up to about 10 ms⁻¹. A theoretical basis for this is given by radar models that are well suited to address dependencies on viewing and environmental conditions. Kudryavtsev et al. (2012a,b) provide a unified framework of roughness *contrast*, which for measurements of SAR normalized radar cross section

(σ_o), is defined as

$$\frac{\sigma_o - \overline{\sigma_o}}{\overline{\sigma_o}}. \quad (1)$$

The overbar denotes a smoothing to lower resolution. Not only is roughness contrast an effective method of highlighting filaments of all shades (cf. Young et al. 2008), but the corresponding radar imaging model (RIM; Kudryavtsev et al. 2005) provides a functional expression that varies linearly with ocean current convergence, and in weak winds, depends nonlinearly on surfactants (e.g., in terms of thickness or elasticity). Contrast also depends nonlinearly on wind speed, in that it varies almost linearly with the inverse of friction velocity squared (Kudryavtsev et al. 2012b).

The functional form of the RIM model suggests that wind stress and surface current convergence can be considered somewhat independently of their prior coupled evolution. In other words, SAR snapshots like Fig. 1 might capture a similar transient pattern of ocean current contrasts in stronger or weaker winds, except that the contrasts themselves are weaker or stronger, respectively. It is then possible to consider an adjustment that offers more uniformity in filament contrast, both within an individual SAR scene and for as many scenes as are available, say, over the GSL. This semblance of uniformity may be helpful to refine the search for transient *Calanus* aggregations (Kenney et al. 2001; Sorochan et al. 2021). Adjusted SAR contrasts can then be interpreted preferentially in terms of ocean current convergence, or perhaps more accurately, as current deformation by a combination of convergence and strain (Rasle et al. 2014).

1.2 Measurement modelling

We introduce measurement modelling as complementary to process-oriented approaches like radar or ecosystem modelling. It is well suited to assess the performance of a SAR contrast adjustment on wind speed, even though a complex dependence on sea state (and other variables) is expected. On one hand, the construction of a measurement model does not specify the processes of interest, although our assessment can be considered *specific* to the choice of GSL measurements. On the other hand, a process model (e.g., Kudryavtsev et al. 2012b) targets a *general* relationship that is often consistent with a broad set of measurements, but again by construction, complex processes must be specified. Formally, ours is also called an observational study (Cochran 1972) that employs correlation measures to identify (Pala-cios et al. 2013; Edelmann et al. 2021) and adjust for measurement dependence.

Using a simple measurement model, we propose to examine a partial, and therefore nonlinear, relationship that focuses on right whale foraging habitat and on filaments that are identified as contiguous SAR contrasts (cf. Young et al. 2008). Following Székely and Rizzo (2009) and Danielson et al. (2020), an attempt is made to quantify the linear and nonlinear components of the SAR contrast and wind

speed relationship. Section 3 describes an identification of filaments and our dependence measures. The relationship between contiguous contrasts and wind speed is examined in Section 4, where an adjustment is applied. Biophysical and statistical aspects are discussed in Section 5 and conclusions are given in Section 6.

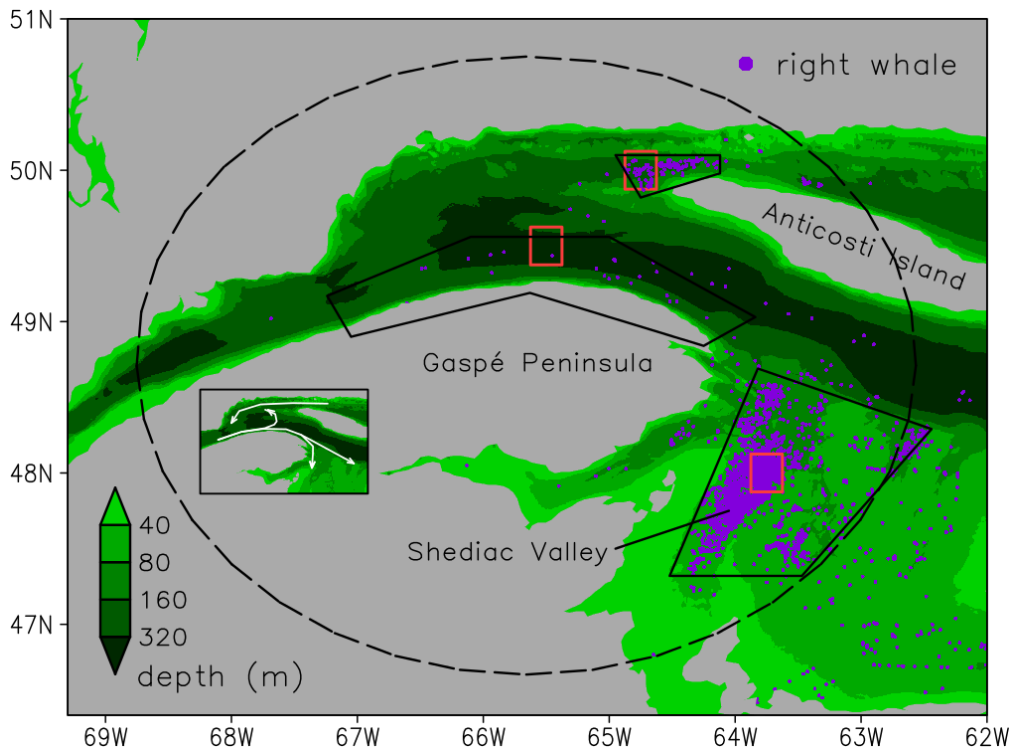


Figure 2: Location of 4900 visual sightings of the North Atlantic right whale (*Eubalaena glacialis*; purple dots) between 2015 and 2020, along with bathymetry (green shading) of the western Gulf of St. Lawrence. Solid black lines encompass the Anticosti (northern), Gaspé (western), and Shediac (southern) domains (see text). Red lines encompass the corresponding ERA5 10-m wind speed gridboxes. White arrows in the inset show the circulation pattern of the western Gulf. Note that sightings are a function of search effort, with uneven coverage in space and time.

2 Data

This section describes right whale sightings for 2015-2020, and SAR and wind data for 2008-2020, for three subdomains in the Gulf of St. Lawrence (GSL). Significant shifts in prey availability during the 2010s (Sorochan et al. 2019) have led the extant NARW population away from their traditional foraging habitats in the Gulf of Maine and Scotian Shelf and toward shallower regions of the GSL, where they were sighted only occasionally prior to 2013 (Kenney 2019). Since 2015, NARWs have been sighted between May and November, more frequently along

the Shediac Valley in the southwestern GSL, and in a small region just northwest of Anticosti Island (Fig. 2). As part of a broad cyclonic circulation in the Gulf (Koutitonsky and Bugden 1991; Lavoie et al. 2016), the Anticosti sightings are furthest upstream (northern domain in Fig. 2) and flow is generally westward along the north shore until it merges with the Gaspé Current (elongated western domain). The relatively fresh St. Lawrence estuary outflow also feeds this coastal current, as it flows around the Gaspé Peninsula. The Gaspé Current is known to transport *Calanus* spp., with periodic intrusions onto the Shediac Valley (the southern domain; Brennan

et al. 2021). The 2019 warm season is notable for having high St. Lawrence river runoff and good SAR coverage.

2.1 Whale Sightings

Typical locations of GSL prey aggregation are taken from two sources of whale sightings. The North Atlantic Right Whale Consortium (NARWC) sightings database (Kenney 2019; NARWC 2021) includes 3265 aerial survey and vessel-of-opportunity right whale sightings (either of a whale group or an individual whale) from 2015 onward in the GSL. A complementary Fisheries and Oceans Canada (DFO) database contains 2586 sightings of right whales (DFO 2020), although this excludes a subset of aerial surveys from the most recent years. Some DFO sightings might have been of dead whales, but this is only recorded in the NARWC data (which reduces the NARWC data from 3265 to 3188). The DFO sightings

are reported in local time and UTC (NARWC sightings are in UTC).

The NARWC and DFO datasets each contain identical sightings separated by only a few minutes and less than a kilometer¹. This highlights that the same observer, or multiple observers, may report on the same whale more than once (and that some whales are counted more often than others, either on the same day or on different days). This observing-effort duplication is retained. Unrelated to effort, the NARWC and DFO sightings are also partially overlapping, so duplicates are omitted if two sightings of the same number of whales occurs within 24 h and 0.01° latitude and longitude. This reduces the combined number of sightings by 874. The remaining 4900 sightings of a group or individual right whale (1712 and 3188; Fig. 2) corresponds to 7591 sightings of individuals. The counts per year are listed in Table 1, with the caveat that 2019 and 2020 sightings are preliminary.

Year	NARW Sightings	SAR Scenes	Scenes with NARWs	Sightings in Scenes
2015	114/343	86	2 (2%)	2/3 (2%/1%)
2016	100/159	53	3 (6%)	6/9 (6%/6%)
2017	1151/2118	83	11 (13%)	165/278 (14%/13%)
2018	1622/2913	105	4 (4%)	31/33 (2%/1%)
2019	1904/2049	188	31 (16%)	669/705 (35%/34%)
2020	9/9	68	0 (0%)	0/0 (0%/0%)

Table 1: Number of Gulf of St. Lawrence NARW sightings (by group/individual), and SAR scenes per year between 2015 and 2020 (the 2019 and 2020 sightings are preliminary). Included are the number of scenes with right whales, and the number of right whale sightings (by group/individual) collocated with those scenes, with fractions of their total in brackets. A sighting is considered to be temporally collocated with a SAR scene if both occur on the same day. Coverage by SAR (of dashed circle in Fig. 2) is from May to December and includes 11 (2008), 24 (2009), 31 (2010), 99 (2011), 63 (2012), 68 (2013), and 62 (2014) scenes prior to 2015.

2.2 Synthetic Aperture Radar (SAR)

The Radarsat-2 C-band (5.3-cm) SAR has been operating since May 2008 in a polar Earth orbit about 800 km above the surface. It is capable of transmitting and receiving in horizontal and vertical (H and V) polarization at incidence angles between 20° (near range) and 49° (far range). GSL coverage is available at a pixel resolution of 100 m or smaller over swaths of more than 300 km. We consider all acquisitions during the ice-free months of May through December of 2008-2020 that overlap with the dashed circle in Fig. 2. This yields 941 SAR scenes using trans-

mit and receive with the same polarization (i.e., HH or VV), and all but three employ a narrow or wide ScanSAR beam mode. Although SAR coverage of the GSL varies somewhat by year (Table 1), sightings coverage is notable in 2017 and 2019, with 2019 having the most sightings (1904), the best GSL coverage (188 scenes), and the best sightings coverage (35%).

We focus on a subset of scenes that provide coverage of the Anticosti, Gaspé, and Shediac domains (Fig. 2) between mid-May and mid-August (i.e., when whales are foraging, but winds are weak and filaments are easier to identify). This subset has 177, 241, and

¹Information about right whale presence and absence is generally sparse, but opportunistic sightings are more frequent closer to shore and during the summer months. Sighting *effort* also depends on observing conditions (e.g., visibility depends on sea state, fog, precipitation, and time of day). Effort increased after 2016 but was affected by COVID-19; no effort corrections are employed here.

237 scenes, respectively (a total of 324 scenes). Initial SAR processing involves reducing the resolution of normalized radar cross section (σ_o) by a smoothing operator that halves resolution on each pass (Koch 2004). This yields scenes at 100-m, 200-m, 400-m, 800-m, 1600-m, 3200-m, 6400-m, and 12800-m resolution (e.g., Fig. 3a,g,l). At 800-m resolution, we also perform a preliminary masking of each scene using the CMOD5 VV ocean wind model (Hersbach

et al. 2007), with the incidence-angle polarization ratio of Zhang et al. (2011) for HH scenes. This is done to partially remove features unassociated with filaments, but to retain a border around any patterns of interest within scenes like Fig. 1. As illustrated in the next section (Figs. 3 and 4), this preliminary masking assumes bounds on σ_o corresponding to a 1-ms^{-1} wind directed parallel to the satellite track, and a 15-ms^{-1} wind directed toward the satellite.

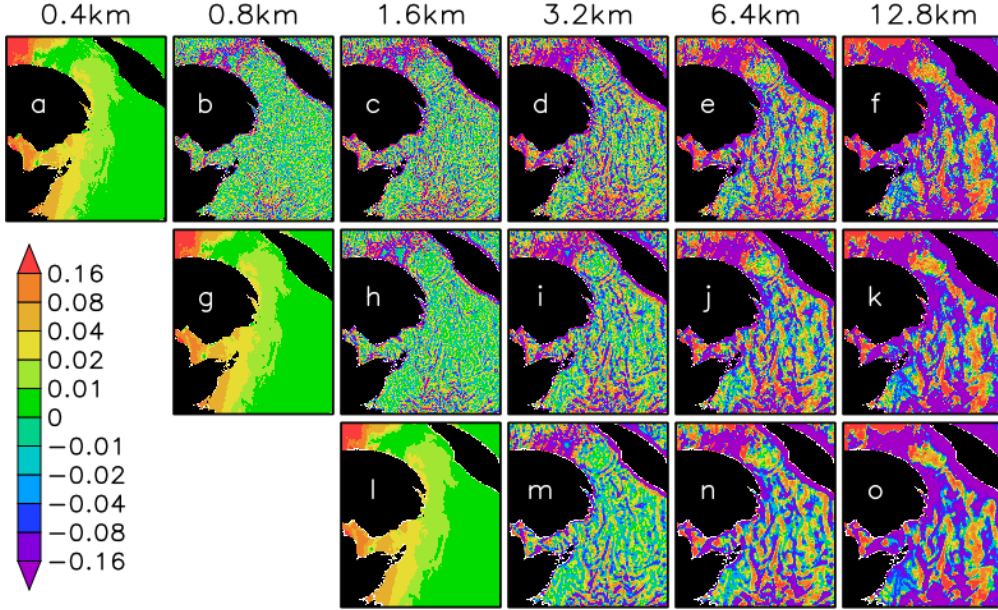


Figure 3: Normalized radar cross section (σ_o) and SAR contrast equation (1) in linear units and at different pixel resolutions for a Radarsat-2 scene (HH) acquired over the Gulf of St. Lawrence on July 26, 2019 (21:59 UTC). Shown are σ_o at a) 0.4-km resolution and contrast at scales up to b) 0.8 km, c) 1.6-km, d) 3.2-km, e) 6.4-km, and f) 12.8-km resolution. Similarly, σ_o is shown at g) 0.8 km with contrast to h-k) 1.6-km through 12.8-km resolution, and at l) 1.6-km with contrast to m-o) 3.2-km through 12.8-km resolution, respectively. Values are given by the colourbar on the left.

2.3 Surface Wind Analysis

A SAR contrast dependence on wind speed is somewhat simpler to interpret if wind speed does not depend on (or assimilate) SAR backscatter. Thus, zonal and meridional wind analyses at 10 m above the surface are taken from the fifth European Centre for Medium-Range Weather Forecasting Reanalysis (ERA5; Hersbach et al. 2020). This reanalysis employs a spectral atmospheric forecast model and a sequential data assimilation system with 137 vertical levels and an effective horizontal resolution of 31 km. The four-dimensional variational (4D-Var) analysis is performed over successive 12-h periods. Bias adjustment of selected observations accommodates systematic differences between the model and observations (Dee 2005). The global atmosphere, land surface,

and ocean surface wave evolution is given at hourly intervals from 1950 onward.

The 10-m wind analyses are obtained from an archive that is resampled at 0.25° , and three sampled locations (red boxes in Fig. 2) are taken as representative ERA5 surface wind estimates for the Anticosti, Gaspé, and Shediac domains. (It is convenient to employ a single gridbox for each domain, as this facilitates measurement model solutions that employ samples at adjacent hours.) We focus on relatively strong SAR contrasts that are indicative of ocean current convergence, perhaps enhanced by the presence of surfactants (Munk et al. 2000; Rascle et al. 2020). Wind speed is thus restricted to $1\text{-}10\text{ ms}^{-1}$ when collocating with SAR contrast in each domain. Values of $1\text{-}3\text{ ms}^{-1}$ are retained here to include strong con-

trasts (i.e., ERA5 weak wind estimates are approximate; cf. Fig. 1).

3 Methods

Aggregations of NARW prey may be only partly localized within a given SAR scene, but the apparent dynamical connections in surface roughness provide more focus for our search. Observations and models motivate a SAR wind speed adjustment, but here, we seek an adjustment that is specific to our

choice of two measurements (i.e., coherent contrasts and ERA5 wind speed in the Fig. 2 domains). First, we confirm that contrast magnitude depends on wind speed. Next, because this partial relationship is expected to be nonlinear (e.g., Kudryavtsev et al. 2012b), we gauge a dependence on wind speed to some power. The power that yields the strongest dependence is taken as appropriate. Our experimental design and proposed adjustment rely on a) an identification of coherent SAR contrasts, and b) measures of the strength of their wind speed dependence.

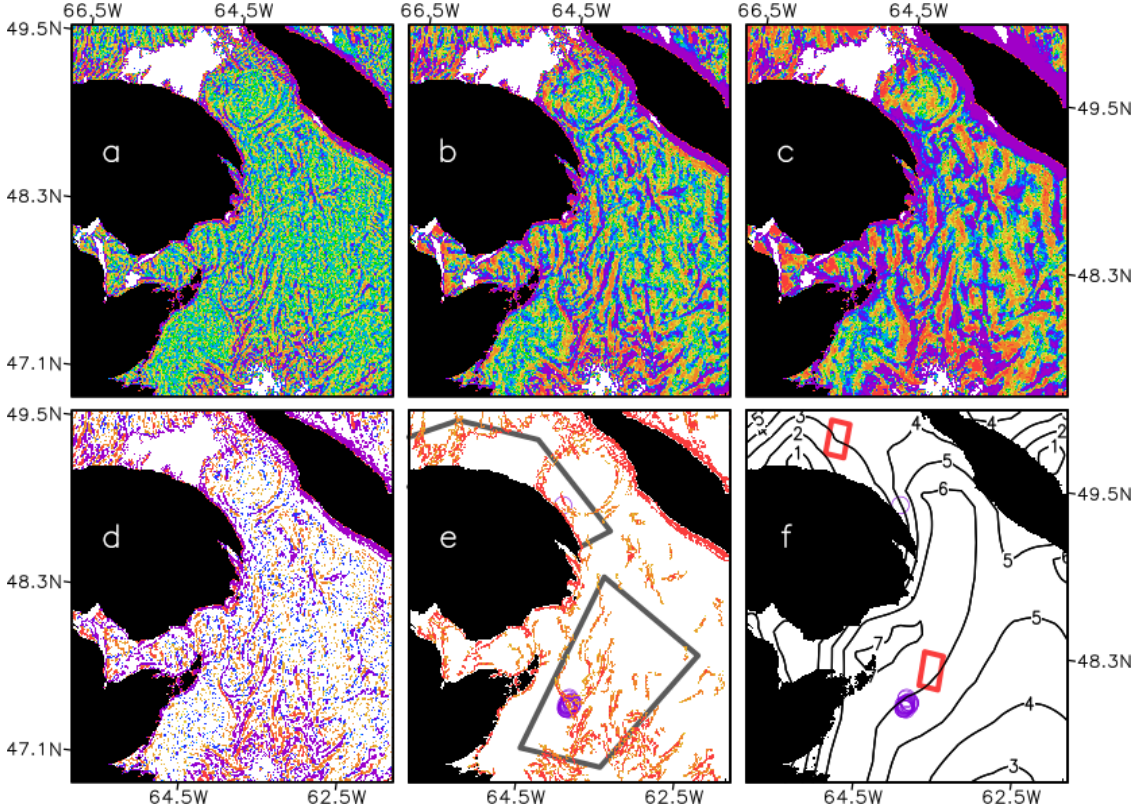


Figure 4: Filament processing and ERA5 wind speed, where (a,b,c) are the same as Fig. 3h,i,j, but include SAR wind speed masking (see text). Also shown are d) an average of (a,b,c) for contrast values of the same sign that are greater than 0.3 in magnitude, e) contrast magnitude for filaments defined by the contiguous values of (d) that cover a distance of at least 10 km, and f) ERA5 10-m wind speed at 1-ms^{-1} intervals. Values are in linear units in (a-e) with colours as in Fig. 3. Included in (e) and (f) are right whale sightings on this day, July 26, 2019 (purple circles), and e) SAR (grey) and f) ERA5 (red) domains of Fig. 2.

3.1 Filament Coherence

In assessing ways to identify roughness features in SAR imagery, Young et al. (2008) note that “manual phenomena identification...is easier following feature extraction...and easier still following pixel aggregation.” Here, SAR contrast in equation (1) is taken to capture (or extract) the features of interest, but in

support of a search (manual or otherwise) for *Calanus* hotspots, coherence (or pixel aggregation) can also be addressed. Although 286 (88%) of the 324 GSL SAR scenes employ VV polarization, a separate HH wind speed adjustment is not considered here because local SAR measurement contrast in equation (1) is given as an HH or VV ratio. We take coherence to be con-

tiguous contrasts that would nearly span a submesoscale eddy (Munk et al. 2000), by a distance of at least 10 km. Following Kudryavtsev et al. (2012b), σ_o and $\overline{\sigma_o}$ can be averages over moving windows of, say, 250-m and 25-km respectively. Although such boxcar averages can include a wide range of finescale structure (i.e., roughly equivalent to the scales between our 100-m and 6.4-km nominal pixel resolutions; Koch 2004), an initial examination of a range of resolution brackets helps to determine the shape and extent of the filaments of interest.

There are 28 possible combinations of σ_o and $\overline{\sigma_o}$ for resolutions between 100 m and 12800 m. A subset of 12 combinations is shown in Fig. 3 for a SAR scene acquired on July 26, 2019. As expected, large scale contrast patterns vary mainly with $\overline{\sigma_o}$, so column panels are similar. However, $\overline{\sigma_o}$ at 800-m (Fig. 3b) and 12800-m (Fig. 3f,k,o) resolution seem to capture not enough or too much of this large scale pattern, respectively. Instead, we opt to define filaments where there is agreement in contrast among, for example, Fig. 4a,b,c. That is, we consider σ_o at 800-m, and $\overline{\sigma_o}$ at 1600-m, 3200-m, or 6400-m pixel resolution. By agreement, we mean an average of these three contrast values, but only where all are positive or negative and larger in magnitude than 0.3. This agreement among three overlapping resolution brackets serves to isolate contiguous contrasts (Fig. 4d), from which filaments are identified that span a distance of at least 10 km (Fig. 4e). To compare with representative values of ERA5 wind speed (Fig. 4f red boxes), we obtain a single value of contrast magnitude for each of the three GSL domains by averaging on the overlap with each SAR scene. Because overlap values are set to zero outside filaments, it is only the values inside filaments that make a nonzero contribution to domain averages.

Figure 4 helps to motivate an adjustment for wind speed across a single SAR scene. Twenty-one right whale sightings are clustered in Fig. 4e (purple circles) along filaments that appear to bound a southward intrusion of the Gaspé Current into the Shediac Valley. Further upstream, between the Gaspé Peninsula and Anticosti Island is the signature of a large anticyclonic excursion of the Gaspé Current (i.e., an Altika pass on this day indicates a positive sea surface height anomaly; not shown). The anticyclonic excursion and Shediac intrusion are collocated with relatively strong wind speed (Fig. 4f) and are weakly delimited by filaments. On the other hand, further south of the whales is a cyclonic eddy surrounded by extensive filaments that are partially masked (Fig. 4a,b,c). Similarly, part of the Gaspé domain is masked where wind speed is weak. Al-

though filaments are extensive where σ_o is reduced, the search for *Calanus* aggregations is likely to be more successful in the presence of whales (Kenney et al. 2001; Baumgartner et al. 2007). In this case, an adjustment that emphasizes the contrasts in strong wind, relative to contrasts in weak wind, seems reasonable.

3.2 Dependence Measures

Székelly et al. (2007) and Székelly and Rizzo (2009) formulate a measure of dependence called distance correlation that is sensitive to nonlinear and non-monotone measurement covariance, and thus extends and complements Pearson correlation. Whereas Pearson correlation is known mainly as a measure of linear dependence, it is also possible to formulate a wavelike measurement model that accommodates both linear and nonlinear dependence (Danielson et al. 2018, 2020). As noted in Section 5, autocorrelation provides a basis for wavelike model solutions. For SAR contrast magnitude (C) and ERA5 wind speed (U) in the domains of Fig. 2, the model, variance, and cross-covariance components are

$$\begin{aligned} C &= t + \epsilon + \epsilon_C \\ U &= \alpha_U + \beta_U t + \epsilon + \epsilon_U \\ \text{Var}(C) &= \sigma_t^2 + \sigma_\epsilon^2 + \sigma_C^2 \\ \text{Var}(U) &= \beta_U^2 \sigma_t^2 + \sigma_\epsilon^2 + \sigma_U^2 \\ \text{Cov}(C, U) &= \beta_U \sigma_t^2 + \sigma_\epsilon^2. \end{aligned} \quad (2)$$

This model introduces linear association (t), nonlinear association (ϵ), and a lack of association (ϵ_C and ϵ_U) as signal-and-noise terms (but whose interpretation is based on signal), with variance σ_t^2 , σ_ϵ^2 , and σ_C^2 and σ_U^2 , respectively. Such a framework can be said to relate measurements with each other, but only by way of what they both measure. Thus, $t + \epsilon$ (in C) and $\alpha_U + \beta_U t + \epsilon$ (in U) capture the total association between C and U , where α_U and β_U are, respectively, an additive and multiplicative calibration of t in U .

Dependence of SAR contrast magnitude (C) on ERA5 wind speed (U) can be measured using both Pearson and distance correlation. A novel decomposition of Pearson correlation [$\rho = \text{Cov}(C, U) / \sqrt{\text{Var}(C)\text{Var}(U)}$] is also permitted by the linear ($\beta_U \sigma_t^2$) and nonlinear (σ_ϵ^2) components of $\text{Cov}(C, U)$. Multiple solutions of each component are given below, based on samples of ERA5 wind speed at intervals from 1 h to 5 h (cf. Section 5). The two key parameters required to solve equation (2) are β_U and σ_t^2 , and for smooth solutions, it is convenient to fix one of these. Although Danielson et al. (2018) fix β_U , here we fix σ_t^2 to the reverse linear regression value of $\text{Cov}^2(C, U) / \text{Var}(U)$.

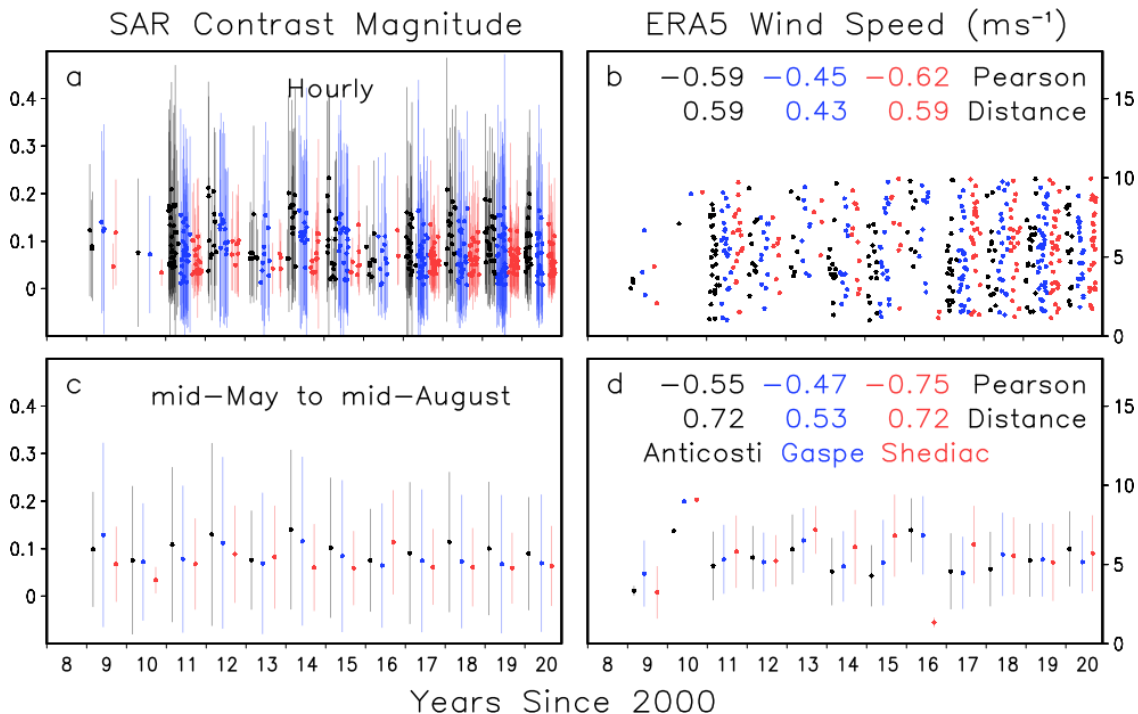


Figure 5: Mid-May to mid-August values of a,c) SAR contrast magnitude (C in linear units) and b,d) ERA5 wind speed (U in ms^{-1}) during 2008-2020 for the Anticosti (black), Gaspé (blue), and Shediac (red) domains of Fig. 2. The Anticosti and Shediac values are shifted by 3.5 months earlier and later, respectively. Shown are averages a,b) for each domain overpass (hourly bin interval) and c,d) for all overpasses between mid-May and mid-August (annual interval; dots with lines above and below of one standard deviation), and the corresponding Pearson and distance correlation values for each domain and time interval.

Dependence within each domain of Fig. 2 is examined by correlating C and U^x , where x is a variable exponent in the range $[-5,5]$. The value x^* that yields the strongest correlation is then taken as an appropriate wind speed adjustment. Because the relationship is inverted (e.g., strong contrast tends to occur in weak winds), we multiply each of three SAR contrast values by $(V/6)^{x^*}$, where V is wind speed interpolated across the scene (i.e., applied to contrast at 800-m resolution, with $\bar{\sigma}_0$ at 1600-m, 3200-m, and 6400-m pixel resolution, including outside the domains of Fig. 2). Also, because neither Pearson nor distance correlation depend on a multiplicative calibration of C (Székely et al. 2007), we include the arbitrary normalization $(1/6)^{x^*}$ as part of this adjustment, so contrast values at wind speeds of 6 ms^{-1} are unchanged.

4 Results

Right whale foraging in the GSL can extend into the fall (NARWC 2021; DFO 2020), but we focus on SAR

scenes during mid-May to mid-August, when winds are lighter and *Calanus* near the surface may be more dense (Brennan et al. 2021; Sorochan et al. 2021). It is easier to pick out a dependence on ERA5 wind speed in the seasonal averages (Fig. 5c,d) than for the individual overpasses (Fig. 5a,b). For example, during years of good SAR coverage, wind speed in the Shediac domain tends to be larger (red dots in Fig. 5d) and contrast magnitude smaller (Fig. 5c) than in other domains. As expected, Pearson correlation is uniformly negative. Distance correlation, which only takes on values between zero and one (i.e., where zero indicates independence), is slightly smaller in the Gaspé domain, perhaps in part because its ERA5 gridbox is less representative of wind speed throughout the corresponding SAR domain (Fig. 2). Nevertheless, Pearson and distance correlation both seem consistent with observations (Espedal et al. 1998; Munk et al. 2000) and model predictions (Kudryavtsev et al. 2012a,b) of a filament contrast dependence on wind speed.

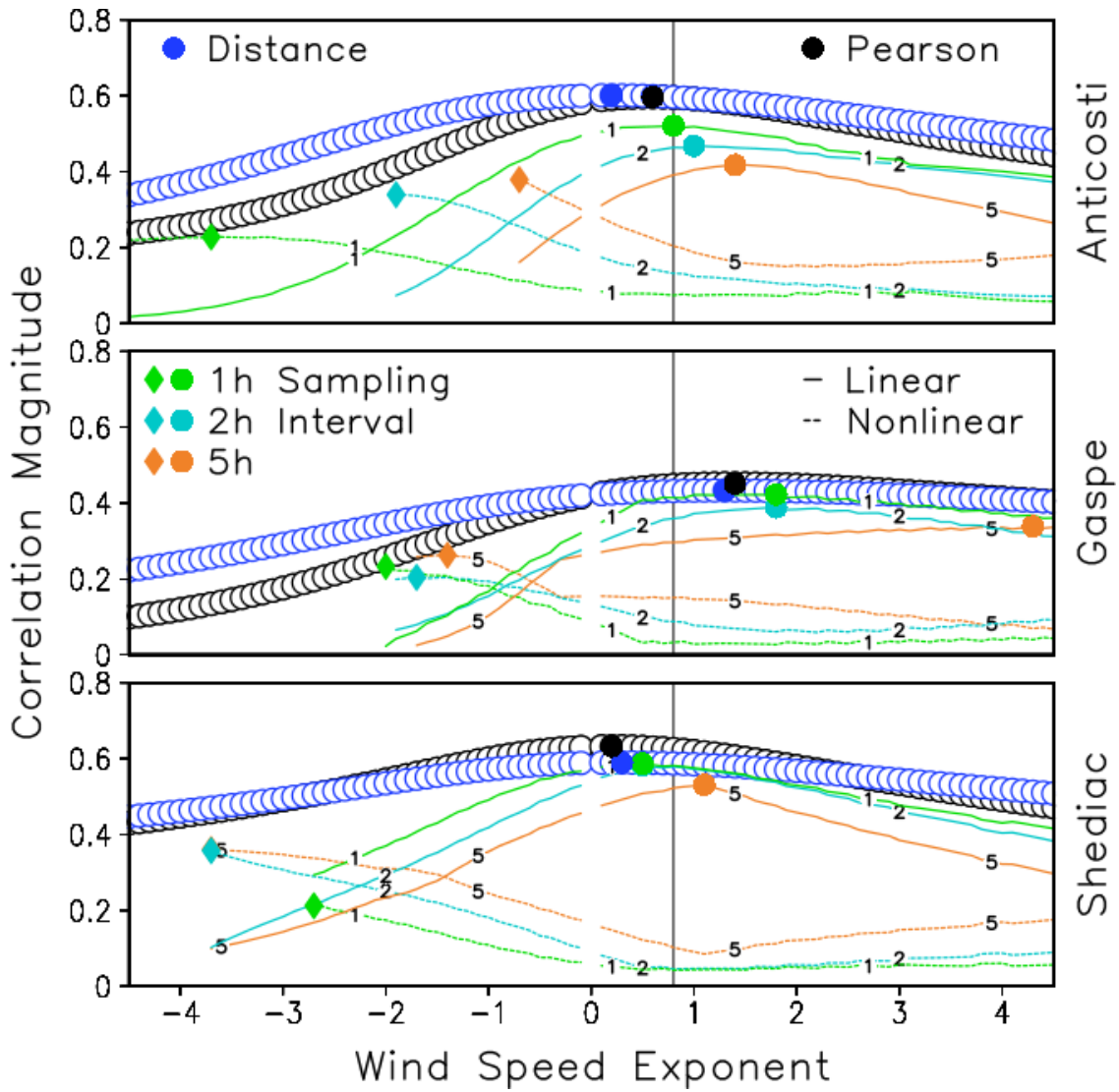


Figure 6: Dependence of Radarsat-2 SAR contrast magnitude (C) on ERA5 wind speed (U^x) as a function of wind speed exponent (x , abscissa) for the Anticosti (top), Gaspé (middle), and Shediac (bottom) domains. Shown are the magnitude of distance correlation (blue circles) and Pearson correlation (black circles), with linear (solid lines) and nonlinear (dashed lines) components of Pearson correlation based on solutions of equation (2) that employ four additional samples of ERA5 wind speed at 1-h (green), 2-h (cyan), and 5-h (orange) intervals. Filled circles and diamonds are maximum values. The vertical line at $x = 0.8$ marks a proposed adjustment.

Figure 6 depicts (C, U^x) correlation magnitude as a function of wind speed exponent (x) for the hourly binned SAR and ERA5 data of Fig. 5a,b. Excluded are values at zero exponent and any component solutions that are unavailable. Across all exponents, distance correlation seems more similar in value (i.e., flatter) than the Pearson correlation. Most correlation minima occur at large negative exponents. Maxima in Pearson and distance correlation (filled circles) are similar to the tabulated values of Fig. 5b (at an exponent of one), but typically occur at an exponent of less than one. At least for the Gaspé and Shediac domains, maxima in Pearson correlation exceed that of distance correlation to a degree expected of bivariate normal data (Székely et al. 2007, their Fig. 1). This is consistent with small skewness of the U^x distributions for x in the range $[0,2]$ (not shown).

Away from their maxima, distance correlation is larger in magnitude than Pearson correlation, which

seems consistent with a greater sensitivity to nonlinear and nonmonotonic dependence (Székely et al. 2007). Solutions of equation (2) at fixed σ_t^2 are not always available, but where there is a nonlinear contribution to Pearson correlation (filled diamonds), the larger value of distance correlation also suggests a nonlinear dependence. Pearson and distance correlation thus seem quite consistent in this study. Both suggest a wind speed adjustment by a small positive exponent that is close to the dominant linear dependence, but is shifted slightly toward a secondary nonlinear dependence that is negative (and moreso for shorter sampling intervals). Also notable is that the linear and nonlinear correlation maxima of Fig. 6 are not directly comparable to the SAR contrast formulae of Kudryavtsev et al. (2012b), but the use of friction velocity instead of wind speed might facilitate a more direct comparison.

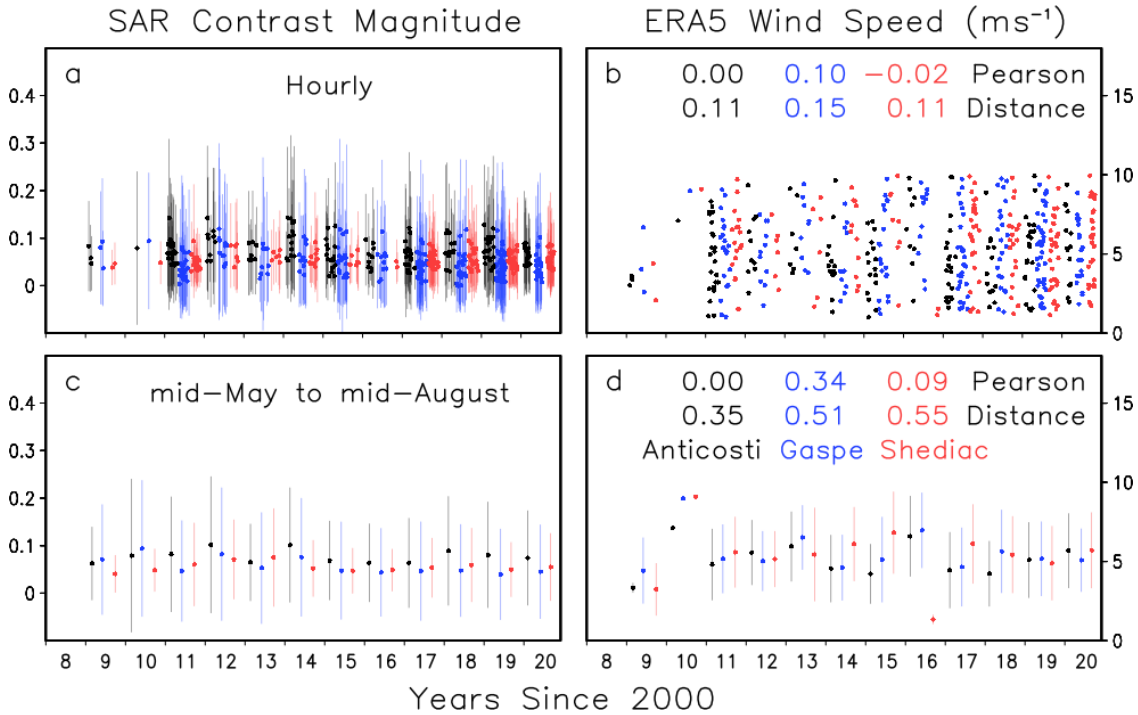


Figure 7: As in Fig. 5, but following an adjustment of SAR contrast magnitude.

The vertical line at $x = 0.8$ in Fig. 6 provides a compromise for the three GSL domains. We multiply SAR contrast by $(V/6)^{0.8}$ to obtain an enhancement or damping, according to whether the ERA5 wind speed collocation (V) is greater than or less than 6 ms^{-1} , respectively. This is done prior to an identification of coherent filaments (Section 3.1) and

yields a reduction in the mean and variance of SAR contrast magnitude (Fig. 7a,c). Whereas Pearson and distance correlation are reduced to values of less than 0.2 (Figure 7b), exponent values greater than 0.8 do not yield a similarly reduced correlation (not shown). This suggests that our adjustment yields a reduction mainly in linear dependence, but also to some extent

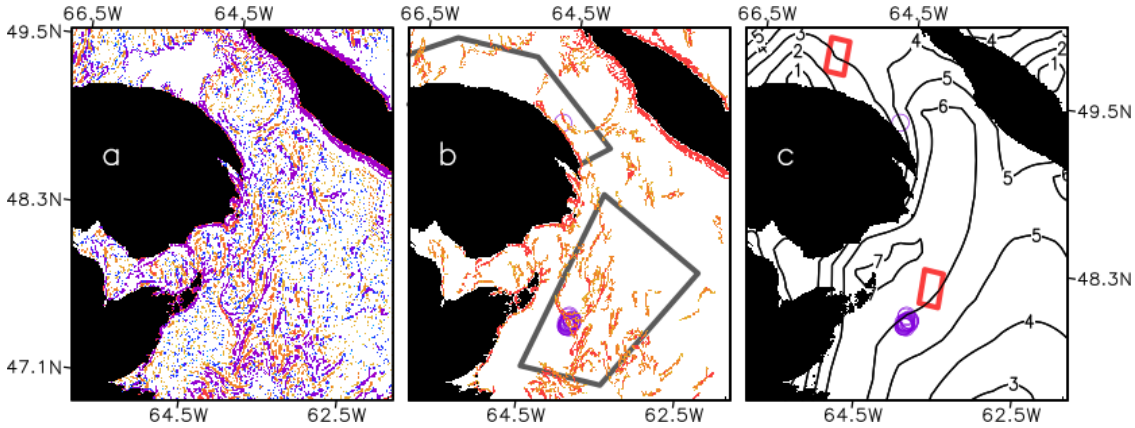


Figure 8: As in Fig. 4d,e,f, but following an adjustment of SAR contrast magnitude.

in nonlinear dependence. For the scene on July 26, 2019 (Fig. 8), filaments oriented along the southward intrusion of the Gaspé Current into the Shediac domain, while small, also become more numerous. A favourable reduction in weak wind contrast at the scene borders is also apparent. In this case, what appear to be the transient watermass boundaries of interest are largely unchanged, but the orientation of the filaments that mark these boundaries is easier to identify. Although SAR contrast variance is still large (Fig. 7a,b), a simple adjustment provides more uniformity across individual scenes.

5 Discussion

Boundary layer circulations may provide an initial organization of filaments, which subsequently gather along watermass strainlines to form extensive connections (Munk et al. 2000; Peacock and Haller 2013; Maps et al. 2015). Dong et al. (2021) propose that zooplankton aggregations can be enhanced by such transient material boundaries. However, at relatively large scales (i.e., larger than an $O[10\text{-km}]$ eddy), the typical SAR signature of biological aggregation, and specifically one that depends on *Calanus* motility, has yet to be proposed (i.e., including the ability of zooplankton to maintain their depth, or otherwise locate themselves within the water column). Sorochan et al. (2021) note that aggregation in the horizontal and vertical are both important, either near the surface or at depth. In turn, aggregations that are nearly collocated with SAR filaments would be expected, as suggested in Fig. 8, as are aggregations delineated by, but not necessarily collocated with, coherent watermass boundaries, like those suggested in Fig. 1. Despite many processes within the water column that SAR is sensitive to (Holt 2004; McWilliams et al. 2009; Shen et al. 2020), contrast in equation (1)

also seems to provide an important spatial reference in a directed search for NARW prey aggregation.

Processes occurring along filaments and material boundaries are also key to this search, although Rascole et al. (2020) emphasize that we are limited in our ability to distinguish actively convergent and decaying filaments. This is needed to identify aggregation processes from space (i.e., to address what aggregation is), but is in part complementary to the question of how best to employ a given platform to measure them. For the scales that we are able to resolve here, a reduction in the nonlinear dependence on wind speed is proposed. Székely and Rizzo (2009) note that a separation of distance correlation into linear and nonlinear components is desirable. Because autocorrelation pertains to the solution of equation (2), which yields this separation in Pearson correlation, a few added comments seem relevant. All correlation values in Figs. 5-7 are obtained under two temporal autocorrelation assumptions: beyond 12 h autocorrelation is weak (more reasonable for SAR contrast than for ERA5 wind speed) and within 12 h it is strong (more reasonable for ERA5 wind speed than SAR contrast). The first assumption permits the use of standard correlation calculations, where it is convenient to treat each timeseries sample as independent. We note that a few SAR scenes are acquired within 12 h of each other in each domain of Fig. 5, but most scenes are well separated.

The second assumption is the basis for solutions of equation (2), by sampling ERA5 wind speed twice before and after each SAR overpass. As in Danielson et al. (2018), a wavelike measurement model can be written involving autocorrelated samples (i.e., where the autocorrelation is wavelike). For sampling intervals of 1 h to 5 h, the outer samples are, respectively, 2 h and 10 h before and after. The hourly ERA5 data thus permit solutions of equation (2), and their

autocorrelation over 12 h is more robust, so this assumption also seems reasonable.

Regarding the origin of nonlinearity in SAR contrast, we expect a confounding (or unobserved) dependence on surfactant properties that is in addition to a dependence on wind speed. The presence of surfactants is also hinted at in the Introduction and a few general comments seem relevant. A review of the state-of-the-art for SAR imaging of surface slicks like crude oil is given by Li et al. (2019) and Huang et al. (2022). SAR is an effective satellite sensor for monitoring of marine surface slicks because of its high-resolution, large areal coverage, and all-weather, day or night capability. Surfactants on the ocean surface tend to dampen the wind-generated surface short gravity and capillary waves that are responsible for the radar backscattering. The dampening is due to increased viscosity and decreased surface tension, which significantly reduces the radar backscatter, resulting in dark patches in SAR images. A challenge for SAR detection of surface slicks is the competition from other natural 'look-alike' phenomena, which may also reduce radar signals thereby resulting in dark areas (e.g., Fig. 1). Look-alike phenomena include low-wind areas, biogenic slicks, rain cells, grease ice or frazil sea ice, surface current shears, wind-shadow areas near coasts, upwelling zones, and internal waves (Alpers et al. 2017).

To identify surface slicks with single-polarization SAR intensity images, earlier studies used threshold methods and a statistical classifier (Fiscella et al. 2000). However, accurate segmentation of dark spots from the clean ocean surface areas is difficult using a simple threshold method for image intensity, because of speckle noise and heterogeneity in the radar backscatter, from near range to far range. Using an adaptive threshold methodology in low winds, dark spot segmentations might contain many look-alikes. Thus, to improve the detection of surface slicks, additional prior knowledge is often needed, such as ocean surface winds etc. (Mera et al. 2012). In any case, these approaches involve complex processes to achieve surface slick detection and classification.

Compared to single-polarization SAR data, which gives the intensity of radar returns, fully polarimetric SAR measures the scattering matrix of targets, providing amplitude and phase data for each image pixel. Therefore, quad-polarization SAR can estimate feature parameters based on polarimetric decomposition theory, which can discriminate different scattering mechanisms related to surface slicks. For example, fully polarimetric, C-band SAR has been also used to identify oil spills, using various polarimetric features like co-polarized phase difference, etc. (Nunziata et al. 2013; Zhang et al. 2011). How-

ever, quad-polarization SAR is not practical for operational monitoring because its coverage is too small (25 or 50 km), whereas single- and dual-polarization SAR is larger (300 km or 500 km). But discrimination of surface slicks from look-alikes is sometimes still not possible, when the wave-damping behaviors are too similar. Even if discrimination could be done, however, surfactants would be expected to contribute to nonlinearity in Fig.6.

6 Conclusions

The presence of NARWs remain among the best indications of high *Calanus* concentrations, but given a supply of *Calanus* in the Gulf of St. Lawrence (GSL), can we also say that prey aggregation is an indication of NARWs? Regarding the delineation of aggregation in measurements, an exploration of surface current deformation by SAR contrast seems well motivated (Kudryavtsev et al. 2012a; Rascle et al. 2014). However, observations and models predict an inverse dependence of SAR contrast on wind forcing and sea state, at least for wind speeds within a range of 1-10 ms^{-1} (Espedal et al. 1998). In the Shediac Valley, for example, where NARWs have been sighted more frequently since 2015, SAR contrast was found to be weak and wind speed strong relative to other GSL regions.

There has been generally improving SAR coverage of the western GSL during the 2010s, with Radarsat-2 capturing about a third of the whale sightings in 2019. A focus on scenes from mid-May to mid-August (2008-2020) permitted a characterization of the SAR-wind relationship when winds are lighter and *Calanus* would have been intermittently aggregated near the surface. Our definition of SAR measurement contrast followed Kudryavtsev et al. (2012b), but employed agreement among three overlapping resolution brackets to isolate contiguous contrasts. Those that spanned a distance of at least 10 km (approaching the eddy length scale; Munk et al. 2000), contributed to an average value of contrast magnitude on the overlap with the Anticosti, Gaspé, or Shediac domains.

Measurement modelling was introduced as a complement to radar imaging models and ecosystem models that are consistent with a broader set of measurements, or that provide a general expression of SAR contrast at the air-sea interface. This study focused on the strength of the relationship between SAR contrast magnitude and ERA5 wind speed to some power, using Pearson and distance correlation (Székely et al. 2007; Székely and Rizzo 2009). Because distance correlation is sensitive to nonlinear and nonmonotonic dependence, it is more consistent with general expressions of SAR contrast (e.g., in-

cluding surfactants, sea state, and wind direction). However, both nonlinear association and a lack of association were also considered, along with linear and nonlinear components of Pearson correlation.

Correlation magnitude was greatest for wind speed to a positive power, and Pearson and distance correlation were consistent. Both were close to the dominant linear dependence, but were shifted slightly toward a secondary nonlinear dependence that was apparent by the nonlinear contribution to Pearson correlation, and by a relatively large value of distance correlation. This provided a simple weighting of SAR contrast whose impact was a correlation of less than 0.2 for all GSL subdomains. By making contrast magnitude more uniform (or less dependent on wind speed), exploration of NARW prey aggregation in a collection of SAR scenes, (and perhaps sun glint, if IR/color images are available) may thus be enhanced. The need to define typical SAR signatures of biological aggregation in the GSL should also be informed by complementary measures of contrast in mass and motion (e.g. [Basedow et al. 2019](#); [Barthelmeß et al. 2021](#)), as well as by observed and simulated measures of *Calanus* spp. availability and

supply ([Gavrilchuk et al. 2020](#); [Brennan et al. 2021](#)).

Acknowledgements

Comments from Hilary Moors-Murphy, Catherine Brennan, Kevin Sorochan, three anonymous reviewers, and the associate editor contributed much to our presentation. We thank the North Atlantic Right Whale Consortium and Team Whale of Fisheries and Oceans Canada for their efforts in collecting and quality controlling the GSL whale sightings. Radarsat data were produced by MacDonald, Detwiler and Associates Ltd. and obtained from the Earth Observation Data Management System of Natural Resources Canada. Sentinel-1 data were obtained from the Copernicus programme of the European Union and the European Space Agency. The ERA5 data were obtained from the Copernicus Climate Change Service (C3S) Climate Data Store. We thank M. Rizzo and G. Székely for providing the distance correlation R package (energy). Funding was provided by the Competitive Science Research Fund (CSRF) and Species at Risk (also denoted SAR) Program of Fisheries and Oceans Canada.

References

- Alpers, W., Holt, B., Zeng, K., 2017. Oil spill detection by imaging radars: Challenges and pitfalls. *Remote Sens. Environ.* 201, 133–147.
- Barthelmeß, T., Schütte, F., Engel, A., 2021. Variability of the sea surface microlayer across a filament’s edge and potential influences on gas exchange. *Front. Mar. Sci.* 8, 1–21, doi:10.3389/fmars.2021.718384.
- Basedow, S. L., McKee, D., Lefering, I., Gislason, A., Daase, M., Trudnowska, E., Egeland, E. S., Choquet, M., Falk-Petersen, S., 2019. Remote sensing of zooplankton swarms. *Sci. Rep.* 9, 1–10, doi:10.1038/s41598-018-37129-x.
- Baumgartner, M. F., Mayo, C. A., Kenney, R. D., 2007. Enormous carnivores, microscopic food, and a restaurant that’s hard to find, *The Urban Whale, North Atlantic Right Whales at the Crossroads*, S. D. Kraus and R. M. Rolland, Eds., Harvard University Press, 138–171, doi:10.2307/j.ctv1pnc1q9.10.
- Brennan, C. E., Maps, F., Gentleman, W. C., Lavoie, D., Chassé, J., Plourde, S., Johnson, C. L., 2021. Ocean circulation changes drive shifts in *Calanus* abundance in North Atlantic right whale foraging habitat: A model comparison of cool and warm year scenarios. *Prog. Oceanogr.* 197, 1–18, doi:10.1016/j.pocean.2021.102629.
- Cochran, W. G., 1972. Observational studies, *Statistical Papers in Honor of George W. Snedecor*, T. A. Bancroft, Ed., Iowa State University Press, pp. 77–90, 2015 reprint doi:10.1353/obs.2015.0010.
- Danielson, R. E., Johannessen, J. A., Quartly, G. D., Rio, M.-H., Collard, F., Chapron, B., Donlon, C., 2018. Exploitation of error correlation in a large analysis validation: GlobCurrent case study. *Remote Sens. Environ.* 217, 476–490, doi:10.1016/j.rse.2018.07.016.
- Danielson, R. E., Zhang, M., Perrie, W. A., 2020. Possible impacts of climate change on fog in the Arctic and subpolar North Atlantic. *Adv. Statist. Clim. Meteor. Ocean.* 475, 1–19, doi:10.5194/ascmo-6-31-2020.

- Dee, D. P., 2005. Bias and data assimilation. *Quart. J. Roy. Meteor. Soc.* 131, 3323–3343, doi:10.1256/qj.05.137.
- DFO, 2020. Whalesightings Database, Team Whale, Fisheries and Oceans Canada, Dartmouth, Nova Scotia [20201202].
- Dong, H., Zhou, M., Hu, Z., Zhang, Z., Zhong, Y., Basedow, S. L., Smith Jr., W. O., 2021. Transport barriers and the retention of *Calanus finmarchicus* on the Lofoten Shelf in early spring. *J. Geophys. Res. Oceans* 126, 1–18, doi:10.1029/2021JC017408.
- Edelmann, D., Móri, T. F., Székely, G. J., 2021. On relationships between the Pearson and the distance correlation coefficients. *Stat. Prob. Lett.* 169, 1–6, doi:10.1016/j.spl.2020.108960.
- Espedal, H. A., Johannessen, O. M., Johannessen, J. A., Dano, E., Lyzenga, D. R., Knulst, J. C., 1998. COASTWATCH'95: ERS 1/2 SAR detection of natural film on the ocean surface. *J. Geophys. Res. Oceans* 103, 24969–24982, doi:10.1029/98JC01660.
- Fiscella, B., Giancaspro, A., Nirchio, F., Pavese, P., Trivero, P., 2000. Oil spill detection using marine SAR images. *Int. J. Remote Sens.* 21, 3561–3566.
- Gavrilchuk, K., Lesage, V., Fortune, S., Trites, A. W., Plourde, S., 2020. A mechanistic approach to predicting suitable foraging habitat for reproductively mature North Atlantic right whales in the Gulf of St. Lawrence. DFO Can. Sci. Advis. Sec. Res. Doc. 2020/034. iv + 47p.
- Hamilton, B., Dean, C., Kurata, N., Vella, K., Soloviev, A., Tartar, A., Shivji, M., Matt, S., Perrie, W., Lehner, S., Zhang, B., 2015. Surfactant associated bacteria in the sea surface microlayer: Case studies in the Straits of Florida and the Gulf of Mexico. *Can. J. Remote Sens.* 41, 135–143, doi:10.1080/07038992.2015.1048849.
- Hersbach, H., Bell, B., Berrisford, P., Hirahara, S., Horányi, A., Muñoz-Sabater, J., Nicolas, J., Peubey, C., Radu, R., Schepers, D., Simmons, A., Soci, C., Abdalla, S., Abellan, X., Balsamo, G., Bechtold, P., Biavati, G., Bidlot, J., Bonavita, M., De Chiara, G., Dahlgren, P., Dee, D., Diamantakis, M., Dragani, R., Flemming, J., Forbes, R., Fuentes, M., Geer, A., Haimberger, L., Healy, S., Hogan, R. J., Hólm, E., Janisková, M., Keeley, S., Laloyaux, P., Lopez, P., Lupu, C., Radnoti, G., de Rosnay, P., Rozum, I., Vamborg, F., Villaume, S., Thépaut, J.-N., 2020. The ERA5 global reanalysis. *Quart. J. Roy. Meteor. Soc.* 146, 1999–2049, doi:10.1002/qj.3803.
- Hersbach, H., Stoffelen, A., de Haan, S., 2007. An improved C-band scatterometer ocean geophysical model function: CMOD5. *J. Geophys. Res.* 112, doi:10.1029/2006JC003743.
- Holt, B., 2004. SAR imaging of the ocean surface, *NOAA synthetic aperture radar marine user's manual*, C. R. Jackson and J. R. Apel, Eds., U. S. Dept. of Commerce, 25–79 (accessed August 2022 at <https://www.sarusersmanual.com>).
- Huang, X., Zhang, B., Perrie, W., Lu, Y., Wang, C., 2022. A novel deep learning method for marine oil spill detection from satellite synthetic aperture radar imagery. *Marine Pollution Bull.* 179, doi:10.1016/j.marpolbul.2022.113666.
- Kenney, R. D., 2019. The North Atlantic Right Whale Consortium database: A guide for users and contributors (accessed January 2021 at https://www.narwc.org/uploads/1/1/6/6/116623219/narwc_users_guide_v.6_.pdf).
- Kenney, R. D., Mayo, C. A., Winn, H. E., 2001. Migration and foraging strategies at varying spatial scales in western North Atlantic right whales: A review of hypotheses. *J. Cetacean Res. Manage.* (special issue) 2, 251–260, doi:10.47536/jcrm.vi.283.
- Koch, W., 2004. Directional analysis of sar images aiming at wind direction. *IEEE Trans. Geosci. Remote Sens.* 42, doi:10.1109/TGRS.2003.818811.

- Koutitonsky, V. G., Bugden, G. L., 1991. The physical oceanography of the Gulf of St. Lawrence: A review with emphasis on the synoptic variability of the motion, p. 57-90. The Gulf of St. Lawrence: Small ocean or big estuary? Can. Spec. Publ. Fish. Aquat. Sci., 113.
- Kudryavtsev, V., Akimov, D., Johannessen, J., Chapron, B., 2005. On radar imaging of current features: 1. Model and comparison with observations. J. Geophys. Res. 110, 1–27, doi:10.1029/2004JC002505.
- Kudryavtsev, V., Myasoedov, A., Chapron, B., Johannessen, J. A., Collard, F., 2012a. Imaging mesoscale upper ocean dynamics using synthetic aperture radar and optical data. J. Geophys. Res. 117, doi:10.1029/2011JC007492.
- Kudryavtsev, V., Myasoedov, A., Chapron, B., Johannessen, J. A., Collard, F., 2012b. Joint sun-glitter and radar imagery of surface slicks. Remote Sens. Environ. 120, 123–132, doi:10.1016/j.rse.2011.06.029.
- Kurata, N., Vella, K., Hamilton, B., Shivji, M., Soloviev, A., Matt, S., Tartar, A., Perrie, W., 2016. Surfactant-associated bacteria in the near-surface layer of the ocean. Sci. Rep. 6, 19123, doi:10.1038/srep19123.
- Lavoie, D., Simard, J. C. Y., Lambert, N., Galbraith, P. S., Roy, N., Brickman, D., 2016. Large-scale atmospheric and oceanic control on krill transport into the St. Lawrence Estuary evidenced with three-dimensional numerical modelling. Atmos.–Ocean 54, 299–325, doi:10.1080/07055900.2015.1082965.
- Li, H., Perrie, W., Wu, J., 2019. Retrieval of oil-water mixture ratio at the ocean surface using compact polarimetry synthetic aperture radar. Remote Sens. 11, 816, doi:10.3390/rs11070816.
- Maps, F., Plourde, S., McQuinn, I. H., St. Onge-Drouin, S., Lavoie, D., Chassé, J., Lesage, V., 2015. Linking acoustics and finite-time Lyapunov exponents reveals areas and mechanisms of krill aggregation within the Gulf of St. Lawrence, eastern Canada. Limnol. Oceanogr. 60, 1965–1975, doi:10.1002/lno.10145.
- McWilliams, J. C., Colas, F., Molemaker, M. J., 2009. Cold filamentary intensification and oceanic surface convergence lines. Geophys. Res. Lett. 36, 1–5, doi:10.1029/2009GL039402.
- Mera, D., Cotos, J. M., Varela-Pet, J., Garcia-Pineda, O., 2012. Adaptive thresholding algorithm based on SAR images and wind data to segment oil spills along the northwest coast of the Iberian Peninsula. Mar. Pollut. Bull. 64, 2090–2096.
- Munk, W., Armi, L., Fischer, K., Zachariasen, F., 2000. Spirals on the sea. Proc. Roy. Soc. Lond. A 456, 1217–1280.
- NARWC, 2021. Identification and Sightings Data of the North Atlantic Right Whale Consortium as of January 2021 (offline archive at New England Aquarium, Boston, Massachusetts, U.S.A.).
- Nunziata, F., Gambardella, A., Migliaccio, M., 2013. On the degree of polarization for SAR sea oil slick observation. ISPRS J. Photogr. Remote Sens. 167, 190–200.
- Palacios, D. M., Baumgartner, M. F., Laidre, K. L., Gregr, E. J., 2013. Beyond correlation: integrating environmentally and behaviourally mediated processes in models of marine mammal distributions. Endang. Species Res. 22, 191–203, doi:10.3354/esr00558.
- Peacock, T., Haller, G., 2013. Lagrangian coherent structures: The hidden skeleton of fluid flows. Phys. Today 66, 41–47, doi:10.1063/PT.3.1886.
- Plourde, S., Lehoux, C., Johnson, C. L., Perrin, G., Lesage, V., 2019. North Atlantic right whale (*Eubalaena glacialis*) and its food: (I) a spatial climatology of *Calanus* biomass and potential foraging habitats in Canadian waters. J. Plankton Res. 41, 667–685, doi:10.1093/plankt/fbz024.
- Rasle, N., Chapron, B., Molemaker, J., Nogueir, F., Ocampo-Torres, F. J., Osuna Cañedo, J. P., Marié, L., Lund, B., Horstmann, J., 2020. Monitoring intense oceanic fronts using sea surface roughness: Satellite, airplane, and in situ comparison. J. Geophys. Res. Oceans 125, 1–22, doi:10.1029/2019JC015704.

- Raschle, N., Chapron, B., Ponte, A., Ardhuin, F., Klein, P., 2014. Surface roughness imaging of currents shows divergence and strain in the wind direction. *J. Phys. Oceanogr.* 44, 2153–2163, doi:10.1175/JPO-D-13-0278.1.
- Raschle, N., Molemaker, J., Marié, L., Nouguier, F., Chapron, B., Lund, B., Mouche, A., 2017. Intense deformation field at oceanic front inferred from directional sea surface roughness observations. *Geophys. Res. Lett.* 44, 5599–5608, doi:10.1002/2017GL073473.
- Shen, H., Perrie, W., Johnson, C. L., 2020. Predicting internal solitary waves in the Gulf of Maine. *J. Geophys. Res. Oceans* 125, 1–22, doi:10.1029/2019JC015941.
- Sorochan, K., Plourde, S., Morse, R., Pepin, P., Runge, J., Thompson, C., Johnson, C. L., 2019. North Atlantic right whale (*Eubalaena glacialis*) and its food: (II) interannual variations in biomass of *Calanus spp.* on western North Atlantic shelves. *J. Plankton Res.* 41, 687–708, doi:10.1093/plankt/fbz044.
- Sorochan, K. A., Plourde, S., Baumgartner, M. F., Johnson, C. L., 2021. Availability, supply, and aggregation of prey (*Calanus spp.*) in foraging areas of the North Atlantic right whale (*Eubalaena glacialis*). *ICES J. Mar. Sci.* 78, doi:10.1093/icesjms/fsab200.
- Székely, G. J., Rizzo, M. L., 2009. Brownian distance covariance. *Annals of Applied Statistics* 3, 1236–1265, doi:10.1214/09-AOAS312.
- Székely, G. J., Rizzo, M. L., Bakirov, N. K., 2007. Measuring and testing dependence by correlation of distances. *Annals of Statistics* 35, 2769–2794, doi:10.1214/009053607000000505.
- Young, G., Sikora, T., Winstead, N., 2008. Mesoscale near-surface wind speed variability mapping with synthetic aperture radar. *Sensors* 8, 7012–7034, doi:10.3390/s8117012.
- Zhang, B., Perrie, W., He, Y., 2011. Wind speed retrieval from RADARSAT-2 quad-polarization images using a new polarization ratio model. *J. Geophys. Res.* 116, 1–13, doi:10.1029/2010JC006522.